Observed physical and environmental causes of scatter in whitecap coverage values in a fetch-limited coastal zone

Adrian H. Callaghan,[1] Grant B. Deane,[2] and M. Dale Stokes[2]

Received 17 July 2007; revised 29 October 2007; accepted 28 February 2008; published 17 May 2008.

[1] Meteorological and oceanographic data along with sea surface images were recorded at a fetch-limited coastal site to investigate the effect of physical and environmental conditions on whitecap coverage *W*. An automated image-processing technique allowed over 100,000 images to be analyzed for *W*. Data analysis showed that many processes influenced *W*. The presence of tidal currents appeared to have augmented values of *W* under certain specific conditions. Analysis of wave spectra indicated the ubiquitous presence of swell propagating northward. Scatter in *W* was markedly absent in mixed seas when the spectral intensity of the wind waves was of the same order of magnitude as the spectral intensity of the swell waves. Swell-dominated seas introduced much more scatter in *W*. *W* was approximately one third lower in swell-dominated seas than in mixed seas. Specifically, steep swell waves (steepness values greater than 0.01) that propagated opposite to wind wave direction appeared to have reduced *W* at wind speeds below approximately 7.5 m s^{-1}, but this effect needs more investigation. The coastal site enabled the possibility of investigating physical and environmental effects on *W* that would otherwise have been more difficult to observe in the open ocean.

Citation: Callaghan, A. H., G. B. Deane, and M. D. Stokes (2008), Observed physical and environmental causes of scatter in whitecap coverage values in a fetch-limited coastal zone, *J. Geophys. Res.*, *113*, C05022, doi:10.1029/2007JC004453.

1. Introduction

[2] Whitecaps are the result of surface gravity waves breaking. When waves break at sea, they trap air in the water column, forming a plume of bubbles which rises up to the sea surface and forms whitecaps. The presence of whitecaps on the sea surface has important implications for a number of oceanographically related processes, some of which include air-sea gas exchange of CO_2, radiative forcing of incoming solar radiation, remote sensing of the ocean surface, and marine aerosol production.

[3] *Monahan and Spillane* [1984] proposed that the gas transfer velocity was proportional to whitecap coverage, and *Woolf* [2005] states similarly that at least a fraction of gas transfer should scale with whitecap coverage. Indeed, the laboratory experiments of *Asher et al.* [1996] showed that there was a linear dependence between the gas transfer velocities of a wide range of gases, including CO_2, and simulated breaking waves.

[4] The high albedo of whitecaps means that they are effective reflectors of incoming solar radiation. This reflectivity effect has consequences for both the Earth's radiative budget and remote sensing of ocean color from space. *Frouin et al.* [2001] found that whitecaps may exert a globally averaged cooling influence on the planet of about 0.03 W m^{-2}.

[5] The accurate retrieval of ocean color products from remote sensing relies in part on developing atmospheric correction algorithms that remove the contaminating effects of the atmosphere and sea surface [*Gordon*, 1997]. Whitecaps result in higher reflectance values than those of the background water, which needs to be taken into account in satellite atmospheric correction algorithms.

[6] An inherent consequence of the presence of whitecaps is bubble bursting. Bubble bursting produces both film and jet droplets which can form sea salt aerosols [*Mårtensson et al.*, 2003]. These primary marine aerosols can affect the global climate through their ability to scatter and absorb radiation [*O'Dowd and de Leeuw*, 2007].

[7] In this paper, we present measurements of percentage whitecap coverage of the sea surface, denoted *W*, from a data set of over 100,000 images taken at a coastal site south of Martha's Vineyard, United States of America. Data presented here correspond to measurements of *W* when the wind was from the northern quadrants. This corresponded to fetch values of between approximately 3 and 20 km. Wind speeds during the period of observation ranged from low (circa 3.5 m s^{-1}) to moderate (circa 12 m s^{-1}). The ratio of water depth to the wavelength of northward propagating swell waves at the experimental site indicated that they were in transition from deep water waves to shallow water waves. The region was also subject to largely east-west tidal flows, resulting in current speeds of up to 0.5 m s^{-1}.

[8] The study of *Anguelova and Webster* [2006] presents a comprehensive summary of previously published wind

[1]Department of Earth and Ocean Sciences, National University of Ireland, Galway, Ireland.
[2]Scripps Institution of Oceanography, University of California, San Diego, California, USA.

0148-0227/08/2007JC004453

speed-only parameterizations of W [see *Anguelova and Webster*, 2006, Figure 1]. For almost all wind speeds, there is a spread of at least 2 orders of magnitude between minimum and maximum model W estimates. While wind speed or wind stress is the main driving force that causes the formation of whitecaps, it has long been known that other factors such as development of the wave spectrum are also important [e.g., *Ross and Cardone*, 1974]. Indeed, *Sugihara et al.* [2007] have explicitly investigated the effect of wavefield conditions on W. They convincingly showed the importance of having coincident wave spectrum measurements when investigating and parameterizing W. There is still, however, a clear need to further investigate what and how environmental and oceanographic processes, other than wind forcing, affect the observed scatter within and between W data sets.

[9] Measuring W in the coastal zone at a location such as the Martha's Vineyard Coastal Observatory (MVCO) on the east coast of the United States has many unique features compared to open ocean measurements of W. The use of a stable platform allows a comprehensive set of images to be collected in a wide range of wind speeds that would not otherwise be possible from a research vessel. Ubiquitous swell in the world's oceans becomes more prominent in the shallow coastal zone because of interaction with the seafloor. Tidal currents often dominate the local current field at a coastal site, and the rise and fall of the tide can be of the order of several meters. Fetch conditions can change rapidly depending on the irregularity of the coastline and the changing wind direction. All of these effects influence the local wavefield and affect wave breaking patterns. With the opportunity of collecting a very large data set of sea surface images along with concurrent oceanographic and meteorological measurements, the coastal zone offers the possibility of evaluating the effects of a wide range of processes on W. While these oceanographic processes are present in the open ocean, the coastal zone acts like a natural laboratory that facilitates the amplification of these processes. The coastal zone thus serves as a link between small-scale laboratory experiments and large-scale open ocean observations.

[10] The primary purpose of this paper is to highlight the various causes of scatter in the measured W for this field study. We also compare our parameterizations of W with previously published models. Section 2 describes the study area and methods, including meteorological and oceanographic data collection (section 2.1), image acquisition and preprocessing (section 2.2), image processing (section 2.3), calculation of W data points (section 2.4), and a brief description of the coastal current regime at the study site (section 2.5). The results and discussion are presented in section 3. Section 3.1 presents a W data set summary. Section 3.2 presents evidence of the tidal effect on W. Section 3.3 discusses the effects of sea state on W. These include the effects of swell waves (sections 3.3.1 and 3.3.2) and the effect of wave age (section 3.3.3) on W. Section 3.4 discusses the applicability of these coastal results to the open ocean. Finally, we make our conclusions in section 4.

2. Study Area and Methods

[11] Data used in this paper were collected during the Surface Processes and Acoustic Communication Experiment (SPACE02) campaign which took place in the autumn of 2002 at a coastal site south of Martha's Vineyard. SPACE02 was an extensive field campaign that included investigation of the acoustical and physical characterization of bubble plumes utilizing the facilities operated by the MVCO. The MVCO is a research facility located on Martha's Vineyard that provides oceanographic and meteorological data for researchers, students and the general public (see the MVCO Web site at http://www.whoi.edu/mvco).

2.1. Meteorological and Oceanographic Data Collection

[12] Meteorological and oceanographic data were obtained from the facilities operated by MVCO. The facilities include a meteorological mast, an acoustic Doppler current profiler (ADCP) and an air-sea interaction tower (ASIT). Figure 1 shows the location of the MVCO site, the positions of the instruments used, and the ASIT. The wind speed data were calculated from a three-axis sonic anemometer located at the South Beach meteorological mast (41°20.996′N, 70°31.606′W) at a height of 12.5 m above sea level. Wind speed values were converted to equivalent wind speed values at a height of 10 m above sea level U_{10} assuming neutral atmospheric conditions using the wind profile power law with an exponent of 0.143 [e.g., *Panofsky and Dutton*, 1984]. Wave spectra were recorded by a Teledyne RD Instruments 1200 kHz Workhorse Monitor ADCP located on the seabed in $\sim$12 m of water, 1.5 km south of Martha's Vineyard and 1.5 km north of the ASIT. Data from the ADCP and meteorological mast are available at the MVCO Web site. The MVCO data processing provides wave statistics and meteorological data every 20 min.

2.2. Image Acquisition and Preprocessing

[13] Images used in this study were collected from 5 to 18 November 2002. A digital camera recorded sea surface images and was located $\sim$15 m above mean sea level on the ASIT and faced a southeast direction. The ASIT is situated in approximately 16 m of water and 3 km from the south shore of Martha's Vineyard. Images were acquired at a rate of 1 Hz during daylight hours, and image resolution was 640 $\times$ 480 pixels (307,200 total pixels). The incidence angle of the camera was set such that the horizon was contained in the field of view.

[14] Because of the fixed location of the camera, some images were contaminated either wholly or partly by sun glint and reflection. Partly contaminated images were cropped in order to remove the contaminated pixels, while entirely contaminated images were discarded. Images were also cropped to remove the horizon and effects in the near field due to the presence of the ASIT. As a result of cropping, the final number of analyzable pixels was $\sim$240,000 per image, which reduced the image dimensions to approximately 565 $\times$ 425 pixels. Before processing, all images were visually inspected and discarded if raindrops on the camera's waterproof housing had degraded the image clarity. Images were not georectified for the effects of oblique photography.

2.3. Image Processing

[15] Images were processed using the automated whitecap extraction (AWE) technique developed at the Department of

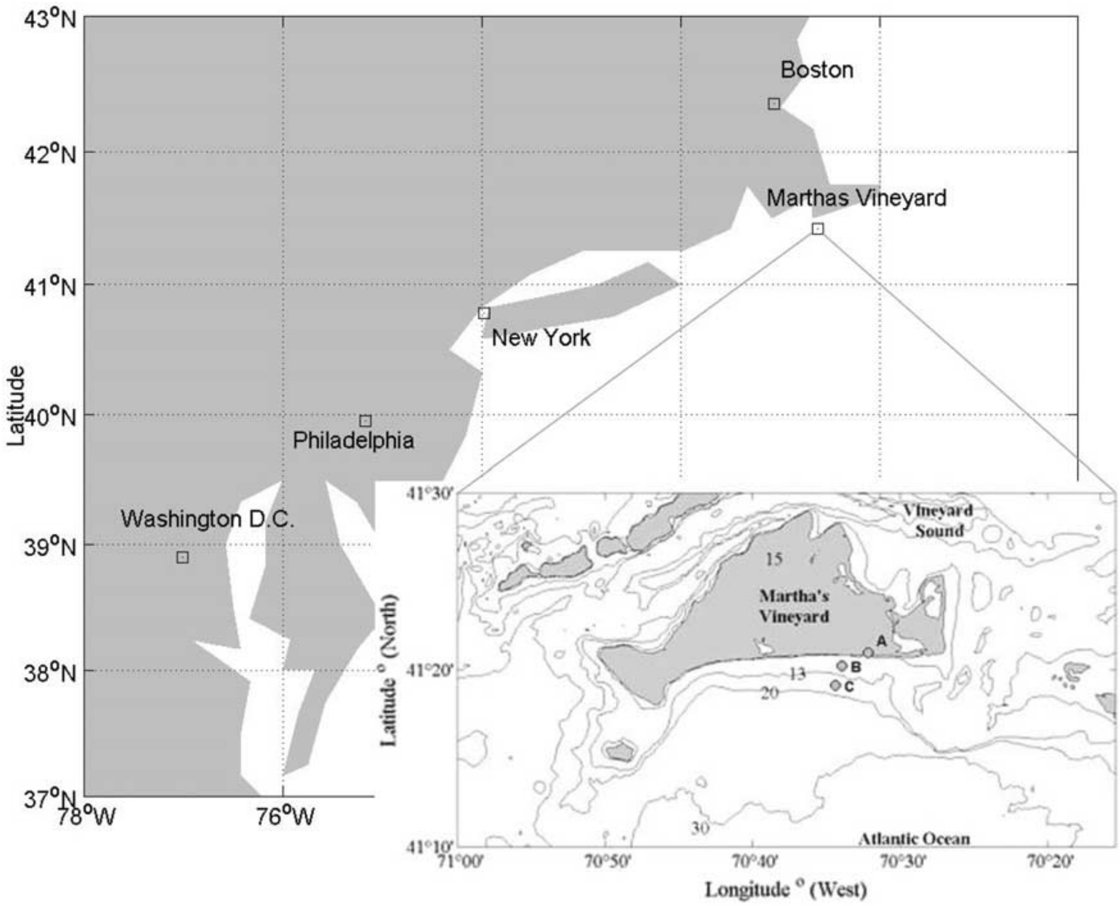

Figure 1. The east coast of the United States with a close-up of the coastal site at Martha's Vineyard (modified from the MVCO Web site) showing the positions of (a) the meteorological mast, (b) the ADCP, and (c) the ASIT. Image courtesy of Janet Fredericks of the Martha's Vineyard Coastal Observatory (see http://www.whoi.edu/mvco).

Earth and Ocean Sciences, National University of Ireland, Galway. AWE uses thresholding of grayscale images as a means to separate whitecaps from background water. The grayscale image pixels initially have intensities in the range of between 0 (black) and 1 (white). Thresholding is a technique whereby pixels in an image are classified into either whitecap or background water on the basis of a critical threshold intensity value. All pixels with an intensity value greater than the threshold are classified as whitecap and assigned an intensity value of 1. The remaining pixels are classified as unbroken background water and are given an intensity value of 0. Pixel classification produces a black and white binary image which clearly identifies the presence (if any) of whitecaps. This method of whitecap classification has been carried out in previous whitecap studies, but typically the threshold for each image was chosen by a human analyst [e.g., *Stramska and Petelski*, 2003; *Asher et al.*, 2002; *Kraan et al.*, 1996]. This manual method has two problems. First, it is extremely time consuming to analyze large numbers of images, and second, it is a subjective process. AWE chooses a threshold for each individual image without user input which enables large number of images to be processed in a relatively short period of time. This method of image analysis was essential for this study, as over 100,000 images were collected and analyzed.

[16] After image preprocessing, AWE proceeds by converting the original RGB image into a grayscale image of double precision. As a result, each pixel in an image has an intensity value in the range of 0 to 1. AWE then iteratively lowers the image threshold in discrete steps from the maximum intensity value of the image to below an intensity value which represents the unbroken background water surface. At each iteration step, the number of pixels with intensities above this new threshold value is calculated. This approach is similar to the image-processing method described by *Sugihara et al.* [2007]. Subsequently, the percentage increase in number of white pixels between each pair of contiguous threshold values is calculated. Figure 2 displays the typical result of the steps described above. It can be seen that at a threshold value of 0.66, a spike in the percentage increase of the detected white pixels begins. Assuming that the intensity values representing the background water are relatively homogenous and lower in value than the intensity of any whitecap present, the intensity value at which the spike begins thus represents the threshold that should be chosen to separate whitecaps from background water. AWE uses derivative analysis to automatically detect the appropriate threshold value. Unlike the method of *Sugihara et al.* [2007], a threshold value is uniquely determined for each individual image.

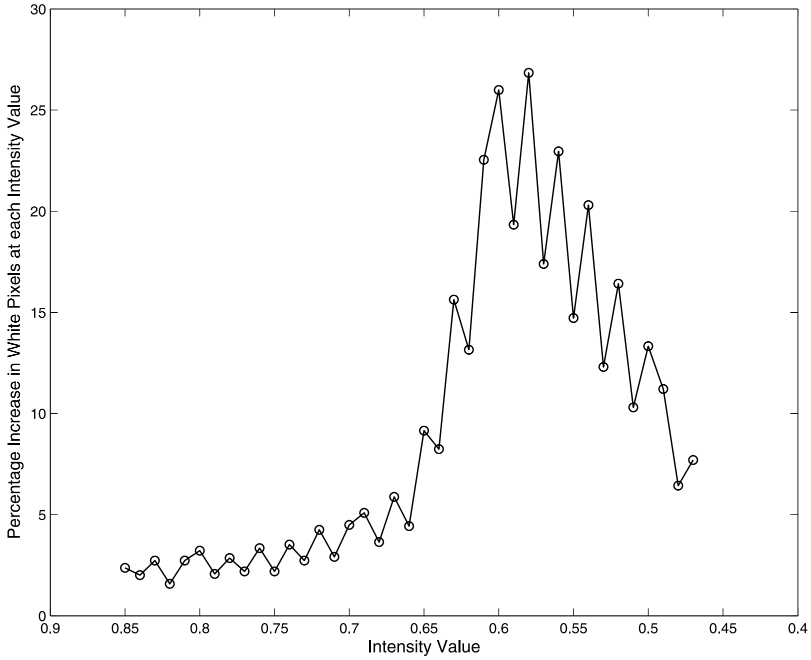

Figure 2. The percentage increase in the number of white pixels at different intensity values.

2.4. *W* Data Point Calculation

[17] Each value of *W* in this study is the result of averaging *W* values from all images acquired in a 20 min time interval. The 20 min sampling period meant that a maximum of up to 1200 images could have been used to compute a single *W* data point. Because of contamination effects of sun glint and sky reflection described in section 2.2, not all values of *W* were from a composite of 1200 images. The minimum number of images used for each *W* data point was 400. *W* data points were calculated at 20 min intervals in order to coincide with the data products provided by the MVCO.

[18] Whitecaps vary immensely both spatially [*Melville and Matusov*, 2002] and temporally, and so it is important to use as many images as possible for each *W* data point. The minimum and maximum number of images used for each value of *W* in this study is larger by a factor of between 16 and 120 compared with three recent studies [e.g., *Stramska and Petelski*, 2003; *Lafon et al.*, 2004, 2007] and comparable to the study of *Sugihara et al.* [2007]. As stated in section 2.2, images from this study were not georectified for the effects of oblique photography. This is a similar approach to *Stramska and Petelski*'s [2003] but is unlike *Lafon et al.*'s [2004, 2007]. *Stramska and Petelski* [2003] performed a statistical analysis demonstrating that their values of *W* were not biased by the oblique image geometry. However, without georectification of images, it is important to analyze as many images as possible for each single value of *W*. Given an approximate timescale of the lifetime of a whitecap from formation to decay of between 5 and 10 s and given an image acquisition rate of 1 Hz, then it is possible that a whitecap present in the foreground of an oblique image which has not been georectified could provide a misleadingly large estimate of *W* for image numbers of $O(10)$.

[19] To demonstrate the importance of processing a large number of images to produce a single *W* data point, we calculated values of *W* using varying numbers of images subsampled from four separate 20 min periods (periods A, B, C, and D). Each of the four 20 min periods contained 1200 images and was subsampled at 17 different frequencies. Table 1 lists the subsampling frequencies and the corresponding number of images selected at each frequency. The lowest subsampling frequency was 0.0084 Hz, which resulted in a subset of 10 images selected from the full set of 1200 images. The highest subsampling frequency was 1 Hz, which resulted in all 1200 images being selected as it coincided with the image acquisition rate. The subsampled images for each frequency were then processed and averaged to yield 17 different values of *W* for each of the four 20 min periods. The resulting 17 values of *W* for each of the four 20 min periods are listed in Table 1. To investigate the convergence of *W* values with increasing subsampling frequency, the percentage difference from the mean *W* value of all 1200 images in each period (PD) was calculated. The mean value of *W* for each period is shown in the last row in Table 1.

[20] The PD for each subsampling frequency for each period is plotted in Figure 3. From Figure 3, it can be seen that the PD oscillates initially before stabilizing around 300 to 400 images. This corresponds to a subsampling frequency of between 0.25 and 0.33 Hz which is adequate to detect whitecaps with lifetimes of 3–4 s. At 300 images, *W* values are within ±4% of the mean *W* value. This number of images is similar to the minimum number of 400 images used for each *W* data point in this study. Figure 3 indicates the necessity of averaging over a large number of images to provide a robust estimate of *W* per 20 min sampling period. It is therefore imperative to collect a large number of images from which to estimate *W*.

2.5. Coastal Current Regime

[21] What follows is a very brief description of the coastal current regime observed at the study site during the period of the experiment. Its aim is to provide the reader with a

Table 1. *W* Values Calculated at Each Subsampling Frequency for All Four 20 Min Periods With Subsampling Frequencies and Corresponding Number of Images Used

Subsampling Frequency, Hz	Number of Images Processed per *W* Value	Period A *W*, %	Period B *W*, %	Period C *W*, %	Period D *W*, %
0.0084	10	0.0144	0.3048	0.5129	1.4101
0.0167	20	0.0193	0.4721	0.4872	1.7089
0.0250	30	0.0140	0.3026	0.4492	1.5160
0.0333	40	0.0207	0.3978	0.5693	1.5576
0.0400	48	0.0262	0.3650	0.7574	1.8658
0.0500	60	0.0196	0.3204	0.6500	1.7293
0.0667	80	0.0236	0.3535	0.7567	1.5183
0.1000	120	0.0200	0.3447	0.7195	1.7129
0.1250	150	0.0208	0.3251	0.6886	1.6272
0.1667	200	0.0246	0.3341	0.7447	1.6320
0.2000	240	0.0231	0.3423	0.7788	1.6571
0.2500	300	0.0223	0.3316	0.7664	1.7021
0.3333	400	0.0238	0.3354	0.7758	1.6692
0.4000	480	0.0241	0.3389	0.7781	1.6838
0.5000	600	0.0230	0.3412	0.7732	1.6934
0.6667	800	0.0234	0.3358	0.7646	1.6754
1.0000	1200	0.0232	0.3362	0.7640	1.6898

basic qualitative description of the currents encountered at the study site during the period of this experiment and is not meant in any way to be a fully quantitative description of all conditions which can occur at the study site.

[22] Measured surface and bottom currents were found to be predominantly tidally influenced with occasional measurable additional influence from wind forcing. This additional wind forcing manifested itself in terms of modified current magnitudes and directions. Both surface and bottom currents measured by the ADCP were predominantly aligned along an east-west axis. Westward currents with a heading of approximately 270° were typical of low tide conditions, and eastward currents with a heading of approximately 90° were typical of high tide conditions. Current magnitudes were directly proportional to the tidal range, and surface currents were typically equal or slightly greater in magnitude than bottom currents.

[23] Measured surface and bottom currents were also found to be modified by the prevailing wind. Westerly winds with magnitudes greater than about 8 m s^{-1} were found to increase the magnitude of the eastward currents during high tide and decrease the magnitude of the westward currents at low tide. The opposite effect was apparent for easterly winds. On occasion, both current magnitude and direction were noticeably influenced by the prevailing wind and deviated from the typical scenario outlined above. For example, at low tide on 18 November, surface and bottom currents indicated relatively weak currents with maximum magnitudes of between approximately 15 and 10 cm^{-1} and headings of approximately 150° and 170°, respectively. Wind speed at this time was circa 12 m s^{-1} and from a direction of 270°. The resultant quasi-southward direction of both surface and bottom currents and relatively weak magnitudes probably reflects the combination of the influence of the westerly wind and the barrier effect of the land-sea boundary of Martha's Vineyard which would inhibit any northward flow.

3. Results and Discussion

3.1. Whitecap Data Set Summary

[24] In this study, we focus on conditions of very short fetch which corresponded to wind directions in the range of between 267° and 55°. This resulted in maximum and minimum values of fetch of approximately 20 and 3 km, respectively. Figure 4a displays *W* as a function of both U_{10} and wind direction, and Figure 4b is a scatterplot of all 101 data points of *W* to U_{10} only. The color code in

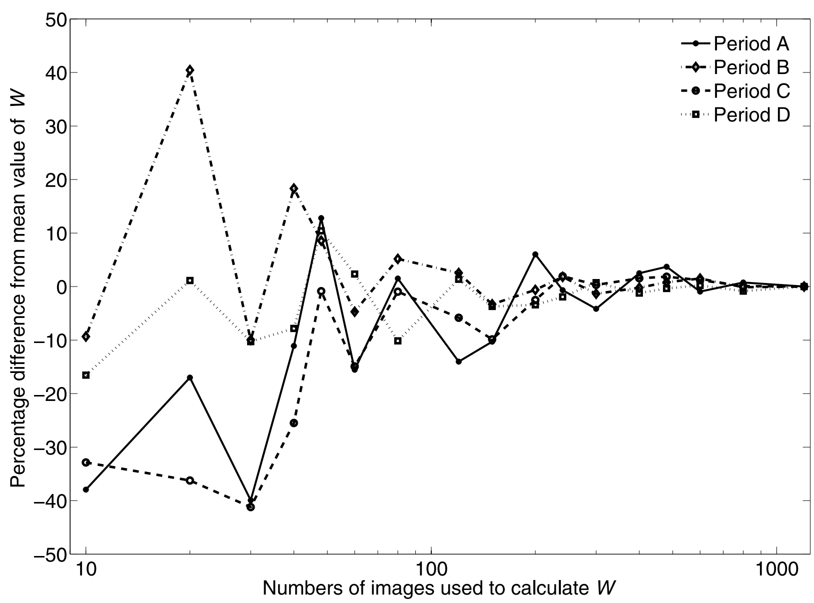

Figure 3. Percentage difference between *W* values and the mean *W* value (PD) calculated using varying numbers of images for four different 20 min sampling periods (periods A, B, C, and D). The mean *W* values were computed using 1200 images from each period.

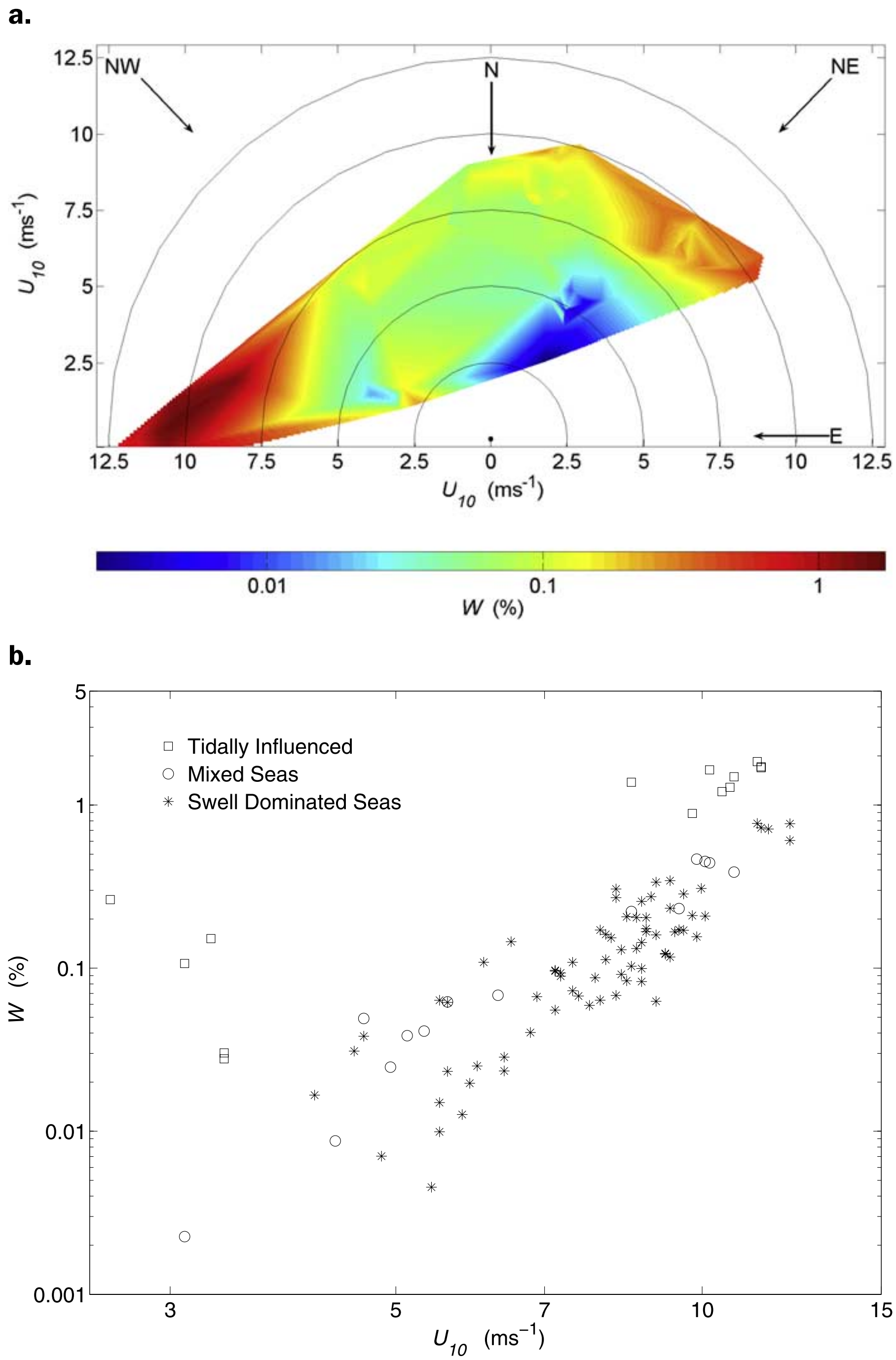

Figure 4. (a) W as a function of wind speed and direction. Wind speed increases radially outward from the origin. Wind direction is given by angle from the vertical at the origin in clockwise rotation. The shading represents W on a log scale. (b) W as a function of wind speed only. Squares, circles, and asterisks correspond to W influenced by unique environmental effects. The effects are discussed in sections 3.2, 3.3.1, and 3.3.2, respectively.

Figure 4a corresponds to values of W. Values of U_{10} increase radially outward from the origin, and the wind direction is given by angle from the vertical at the origin in clockwise rotation. The extreme left, center, and right of the x axis correspond to westerly (270°), northerly (0°), and easterly (90°) winds, respectively. From both plots, it can be seen that W generally increased with increasing wind speed as expected. In Figure 4b, the W data points are represented by three symbols. Each symbol corresponds to a particular set of influencing environmental conditions which are discussed in sections 3.2 and 3.3.

3.2. Tidal Influence on W Values

[25] The most striking feature of Figure 4b is the conspicuously high values of 14 W data points (plotted as squares) at wind speeds of less than 4 m s^{-1} and wind speeds

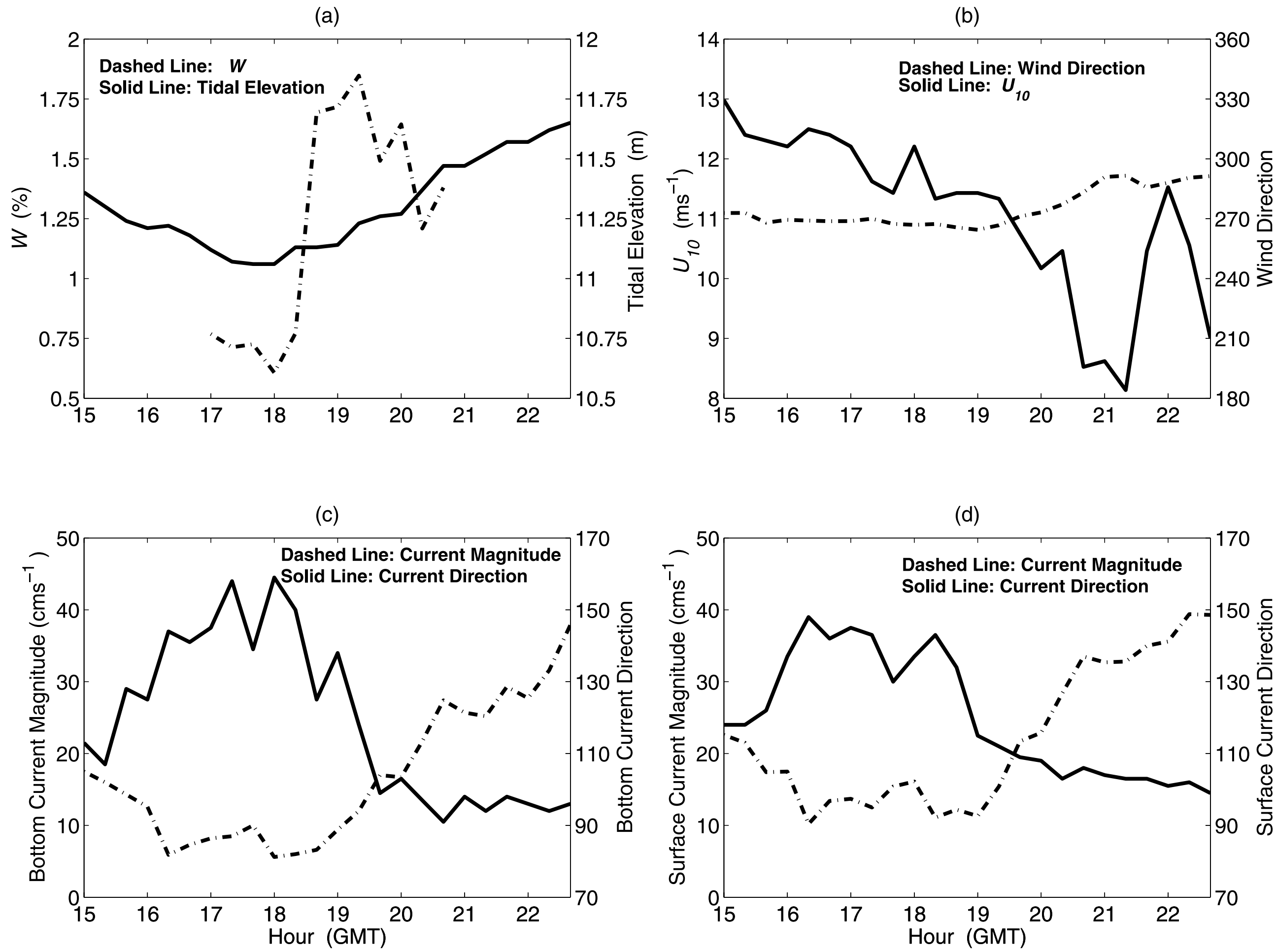

Figure 5. Display time series of meteorological and oceanographic conditions for 18 November. (a) The dashed line represents W, and the solid line represents tidal elevation. (b) The dashed line represents wind direction, and the solid line represents U_{10}. (c) The dashed line represents the magnitude of the current near the seabed, and the solid line represents the current direction as measured by the ADCP. (d) The dashed line represents the magnitude of the current near the surface, and the solid line represents the current direction as measured by the ADCP.

of between 9 and 12 m s^{-1}. From Figure 4a, it can be seen that these relatively high values both occurred when the wind was from a westerly direction. These high values were first apparent on a time series plot of W from 18 November, shown here in Figure 5a. Immediately obvious was the jump in W from 0.77% to 1.69% between successive 20 min averages beginning at 1820 (UTC) shown on the x axis of Figure 5a. Meteorological and oceanographic data 2 h either side of the W measurements are included in Figures 5a, 5b, 5c, and 5d. Surprised by the rapid increase in W, we plotted time series of U_{10} and wind direction, current magnitude, and direction for both the top and bottom ADCP bins and also the tidal elevation for the same period of time. These time series are depicted in Figures 5b, 5c, and 5d. Figure 5b shows wind speed for this time had been steadily decreasing. Wind direction was from 270° and had not changed direction during the preceding 10 h. The only notable coincident changes in environmental conditions that we measured for this time occurred in the tidal elevation and the current velocity. The tide changed from a falling tide to a rising tide, which was reflected in the change in direction and magnitude of both the surface and bottom currents as measured by the ADCP. Both the surface and bottom currents changed from a heading of approximately 170–150° to a new heading of approximately 90–100° accompanied by an increase in current magnitude. This new eastward current heading was aligned with the westerly wind direction and the direction of the higher-frequency portion of the wave spectrum.

[26] Intrigued by these findings, we searched for a similar combination of environmental conditions during our measurement period. On 14 November, a large increase in W was accompanied by an almost identical set of environmental conditions as occurred on 18 November. At the time of the sharp increase in W on 14 November, wind speed was decreasing, wind direction was constant and from 285°, and the tide was changing from a falling tide to a rising tide. The shift in tidal regime caused an increase in current magnitude and a reversal of current direction from an initial heading of 270° to a subsequent heading of 90°. Similarly to what happened on 18 November, this resulted in a directional alignment of wind and currents. Wind wave direction for this time from the ADCP measurements was unclear, but a

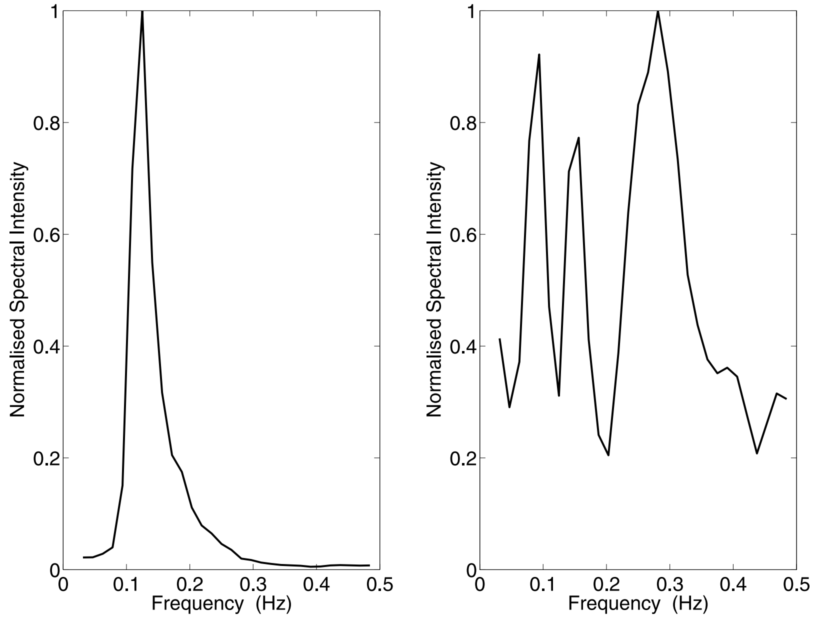

Figure 6. (a) A normalized 1-D wave spectrum from 12 November. The spectral peak frequency at 0.125 Hz corresponds to northward propagating swell. No discernible wind wave-generated peak frequency is present. This spectrum was typical of wave spectra recorded during the course of *W* measurements. (b) A normalized 1-D wave spectrum from 18 November. There are three well-defined peak frequencies evident. Those peaks at 0.09 and 0.16 Hz correspond to swell waves and a decaying wind sea from a wind event earlier in the day, respectively. The third peak frequency at 0.28 Hz corresponds to locally generated wind waves.

visual inspection of the images revealed the presence of a high-frequency wave train propagating eastward.

[27] Measurements of *W* in the presence of recorded tidal currents are scarce. In their coastal study to quantify wave energy dissipation, *Kraan et al.* [1996] measured *W* from actively breaking waves. During their field campaign, they encountered very strong tidal currents of up to 1 m s^{-1}. Contrary to this study, their concurrent measurements of *W* were lower during times of strong tidal currents than at other times. However, they do not state in which direction the tidal currents were propagating and whether they were aligned with the wind direction or not. In light of this, it is difficult to compare their data with the data from this study. However, from the evidence presented in Figures 5a, 5b, 5c, and 5d, we believe that the interaction of the local wavefield aligned with the wind direction and tidal currents produced a marked increase in *W* which could not be explained by any other measured environmental parameter.

3.3. Influence of Sea State on *W*

[28] The remaining 87 data points in Figure 4b denoted as asterisks and circles are broadly separated into two categories. The asterisks represent *W* values measured when the seas were swell dominated, and the circles represent *W* values measured during mixed seas. Examination of the wave spectra for the period of our measurements revealed the ubiquitous presence of swell propagating in a northward direction throughout the duration of this experiment. Directional differences between the wind and swell waves ranged between 70° and 180° for data presented here. Of the 87 spectra examined, only 14 had identifiable peak frequencies that could be attributed to locally wind-generated waves. This was probably due to the short fetch at this site for northerly winds and a steepening of the long waves due to the relatively shallow mean depth of ∼12 m at the wave measurement site. While these 14 spectra still indicated the presence of swell waves, the spectral intensity of both the swell waves and the locally generated waves were of the same order of magnitude (see Figure 6b as an example). For this study, these points are termed mixed sea data points and are displayed as circles. For the other 73 wave spectra examined, the spectral intensity of the swell waves was much greater than that of the higher-frequency portion of the wave spectrum to the extent that no identifiable peak frequency was present which could be accurately attributed to locally wind-generated waves.

[29] Figures 6a and 6b display representative spectra from swell-dominated seas and mixed seas, respectively. Figure 6a is the 1 d frequency spectrum from 12 November showing a single distinct peak frequency at 0.125 Hz. Swell wave direction was toward 360°, and wind direction for this time was from 30°. Figure 6b displays an example of a trimodal sea with frequency peaks at approximately 0.09, 0.16, and 0.28 Hz from 16 November. Each frequency peak was examined in relation to wind history. The lowest-frequency peak corresponded to the ubiquitous northward propagating swell. The frequency peak at 0.16 Hz was attributed to a wind event earlier in the day. Both these peak frequencies were rejected as representing wave trains which were not locally generated. The peak at 0.28 Hz was chosen to represent the locally generated wind waves.

3.3.1. Scatter in *W* Due to Presence of Swell

[30] Figure 7 displays the mixed sea *W* data points only. These 14 data points came from 2 d, 5 and 16 November

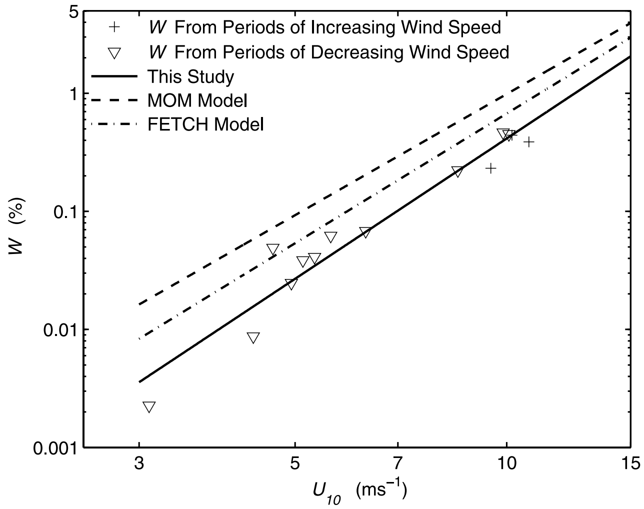

Figure 7. *W* for days when wave spectra exhibited peak frequencies corresponding to locally wind-generated waves (termed mixed sea data points). Plus signs represent *W* when wind speed was increasing. Triangles represent *W* for decreasing wind speed. The solid line is the power law regression on the data. The dashed line corresponds to MOM, and the dash-dot line corresponds to FETCH.

2002. The solid line represents the least squares power law fit, and the resulting regression with r^2 value is

$$W = 4.66 \times 10^{-5} U_{10}^{3.95} \qquad r^2 = 0.94. \tag{1}$$

[31] Many *W* to U_{10} relationships exist in the literature [e.g., *Monahan*, 1971; *Wu*, 1979, 1988; *Monahan and O'Muircheartaigh*, 1980; *Zhao and Toba*, 2001; *Stramska and Petelski*, 2003; *Lafon et al.*, 2004]. In Figure 7, we include the widely quoted model of *Monahan and O'Muircheartaigh* [1980, hereinafter referred to as MOM] (dashed line) as representative of open ocean conditions and the coastal model of *Lafon et al.* [2004, hereinafter referred to as FETCH] (dash-dot line) as comparisons to our data.

[32] The data points denoted as plus signs represent those measurements of *W* when wind speed was increasing. The triangles represent measurements of *W* when wind speed was decreasing. The majority of the data points in Figure 7 were collected in conditions of decreasing wind speed. As only three data points represent conditions of increasing wind speed, it is difficult to make any inferences on the effect of increasing or decreasing wind speed on these values of *W*. Both the MOM and FETCH models overestimate *W* from this study. This is perhaps to be expected, as fetches were very different for each of the three data sets. The majority of the data points that lead to MOM were from the open ocean. The FETCH model data points correspond to fetch values of approximately 60 km. Values of fetch for the data points presented in Figure 7 were less than 6 km. Similarly, both the FETCH model and equation (1) are seen to converge gradually with MOM with increasing wind speed. One important feature of Figure 7 to note is the lack of the characteristic scatter found in many whitecap data sets. The number of data points plotted is only 14, but it must be noted that the combined number of images analyzed to produce these data points was 13,704. It may be possible that the lack of scatter could be attributed to the relatively similar wind directions on 5 and 16 November which were from the northeast quadrant at time of image acquisition. The lack of characteristic scatter, combined with the results of the convergence test in section 2.3, however, leads us to the suggestion that when the influence of factors other than wind forcing on *W*, such as currents and swell, is minimal, using large data sets of images could provide accurate wind speed-only parameterizations of *W*. More *W* data points in mixed or pure wind seas are needed to further investigate this.

[33] Figure 8 is a plot of *W* to U_{10} of the swell-dominated *W* data points only. Plus signs represent measurements made when the wind was rising, and triangles represent measurements made when the wind was decreasing. The solid line corresponds to the least squares power law fit of all the data points, and the resulting regression with r^2 value is

$$W = 2.99 \times 10^{-5} U_{10}^{3.95} \qquad r^2 = 0.74. \tag{2}$$

[34] It is easy to see that the swell-dominated data points in Figure 8 exhibit more scatter in comparison to Figure 7. The scatter in the data is greatest below about 7.5 m s^{-1}, which is a common feature of *W* data sets. This may be due to the fewer numbers of whitecaps present at low wind speeds [*Stramska and Petelski*, 2003]. It might be expected that values of *W* would have been dependent on a rising or falling wind speed with higher values of *W* for a falling wind in comparison to a rising wind at a given wind speed. However, the partitioning of the data into rising and falling winds does not seem to reduce the scatter, and it certainly does not explain the higher degree of scatter in the data points below 7.5 m s^{-1}.

[35] The additional scatter suggests that the effect of wind forcing and wave breaking patterns are different in swell-dominated seas than in mixed seas. *Dulov et al.* [2002] conducted a study to investigate what spectral range of

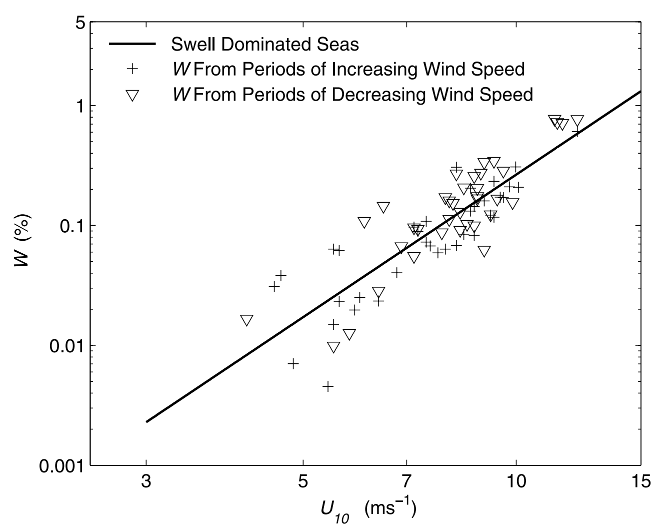

Figure 8. *W* for swell-dominated seas only. Plus signs represent values of *W* when wind speed was increasing. Triangles represent values of *W* for decreasing wind speed.

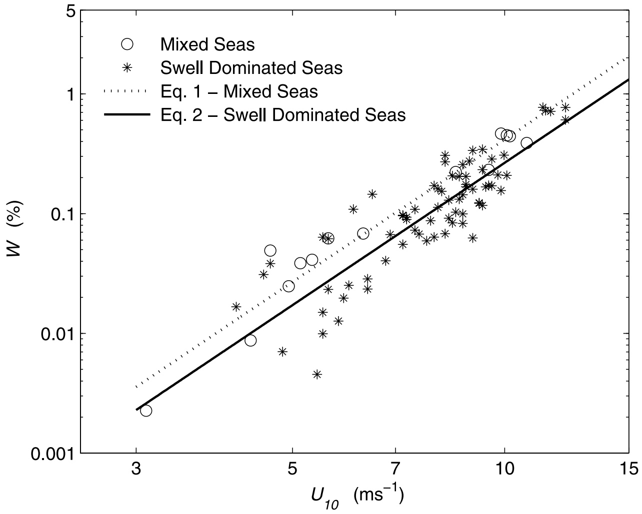

Figure 9. Composite plot of W displayed in Figure 7 (represented by circles) and W displayed in Figure 8 (represented by asterisks). The dotted line represents equation (1), which is the power law regression on the mixed sea W (circles only). The solid line is the power law regression on the swell-dominated W (asterisks only).

breaking waves contribute to W and what influence the waves at the spectral peak frequency had on W. They found that for pure wind seas, 90% of W arose from the breaking of waves with frequencies twice or greater than that of the spectral peak frequency. For the case of mixed seas (where more than one spectral peak frequency was identified), this trend was even more pronounced [see *Dulov et al.*, 2002, Figure 2]. The waves at the spectral peak frequency of the longer waves strongly modulated the occurrence of breaking. Wave breaking was enhanced at the crests of the longer waves and suppressed at the troughs of the longer waves. With the observed effect that long waves strongly modulate the patterns of breaking waves [*Dulov et al.*, 2002], it is reasonable to assume that a wind speed-only parameterization of W would exhibit more scatter in swell-dominated seas than in mixed or swell-free seas. From the results presented here, an accurate parameterization of W with only U_{10} in a coastal zone would be more robust in the absence of swell waves.

3.3.2. Effect of Swell Waves on the Magnitude of *W*

[36] Figure 9 allows a direct visual comparison between the swell-dominated data points (asterisks) and the mixed sea data points (circles). The dotted line represents equation (1), and the solid line represents equation (2). It can be seen that while the mixed sea data points are contained within the scatter of the swell-dominated data points, they tend to lie at the upper end of values of W at given wind speeds. This trend is reflected in the regression relationships for each data set contained in equations (1) and (2). While the slopes of equations (1) and (2) are similar, the scaling factor of equation (2) is approximately one third less than that of equation (1). Our initial thoughts were that this might be indicative of rising and falling wind speeds. However, since segregation of the 73 swell-dominated data points into the two different wind categories in section 3.3.1 revealed no obvious trend, this phenomenon might not be able to explain the differences between the two regressions. The difference between equation (1), representing mixed sea data points, and equation (2), representing swell-dominated data points, may indicate that wave breaking is suppressed somewhat in the presence of an energetic swell. This is similar to the findings of *Sugihara et al.* [2007] that values of W were lower for a given wind speed in swell-dominated seas than in pure wind seas. This effect seemingly did not depend on the direction of the swell waves relative to the wind waves.

[37] In their laboratory study, *Mitsuyasu and Yoshida* [2005] investigated the behavior of a variety of air-sea interactions in the presence of opposing swell. One of the investigated phenomena was the modification of wind-generated waves by coexisting mechanically generated opposing swell waves. They found that in the presence of opposing swell, the wind waves had an increased spectral energy in comparison to the conditions when there was an absence of coexisting opposing swell waves. This effect was found to be more pronounced with increasing fetch. They also found that the opposing swell caused an intensification of the growth of the wind waves, resulting in a shift of the wind wave peak frequency to lower frequencies. Conversely, many laboratory studies have shown that the energy of shorter wind-generated waves is attenuated in the presence of longer swell waves traveling in the same direction [e.g., *Phillips and Banner*,1974; *Donelan*, 1987; *Chu et al.*, 1992; *Chen and Belcher*, 2000]. The average spectral intensity of the waves at the higher end of the frequency spectrum tends to be attenuated in the presence of longer waves traveling in the same direction.

[38] While no universal theory has been developed to reconcile the findings of these authors, one common aspect in all studies is that an increase in the slope or steepness of the swell waves amplifies the wave-wave modulation. *Mitsuyasu and Yoshida* [2005] found that swell waves with ratios of wave height to wavelength below 0.01 had little effect on wind waves. However, above steepness values of 0.01, the influence of the swell waves on the wind waves was very apparent. At steepness values of approximately 0.034, there was an increase of approximately 40% in the energy of the wind waves. Evidence to support the laboratory findings for both cases of aligned and opposed sets of waves in the field are lacking. *Dobson et al.* [1989], *Hanson and Phillips* [1999], and *Violante-Carvalho et al.* [2004] did not find any evidence for the modification of the shorter wind-generated waves in the presence of longer swell waves.

[39] In the controlled laboratory environment, swell waves are relatively steep in order to exaggerate any effects of wave-wave interaction [*Mitsuyasu and Yoshida*, 2005]. In the open ocean, the steepness of the long waves may not be sufficient to confirm the findings in the laboratory. In the finite-depth coastal environment at MVCO, however, the longer waves are in transition between deep water waves to shallow water waves. This transition is accompanied by a reduction in wavelength and phase speed, an increase in wave height, and therefore an increase in wave steepness. Any wave-wave modulation effect observed in the laboratory might therefore be more easily observed in a shallow coastal zone.

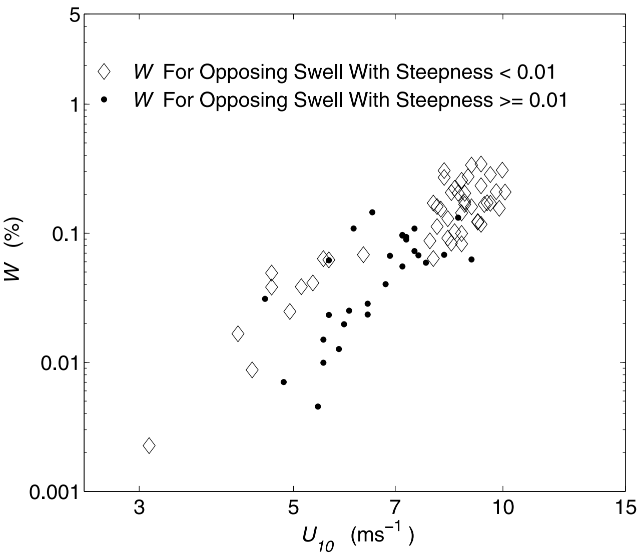

Figure 10. *W* when swell was opposed to wind direction. Dots represent *W* when the swell wave steepness was greater than or equal to 0.01. Diamonds represent *W* when the swell wave steepness was less than 0.01.

[40] Using the formulation of *Mitsuyasu and Yoshida* [2005], we found that typical values for swell wave steepness for the present study ranged between 0.002 and 0.026. This range of steepness values is similar to the range of steepness values of the long waves generated in the laboratory by *Mitsuyasu and Yoshida* [2005] and includes the critical steepness value of 0.01 noted above. Using the findings of *Mitsuyasu and Yoshida* [2005], we would therefore expect the shorter wind waves to have an amplified spectral energy for those values of long wave steepness greater than 0.01. At this point, it is important to clarify that the mechanism by which the short wave amplification occurred in the laboratory, as suggested by *Mitsuyasu and Yoshida* [2005], was via an increase in wind stress due to the presence of the longer swell waves. An increase in spectral energy of the wind waves may also, however, suggest a decrease in energy dissipation through a reduction in wave breaking. We would therefore expect to see smaller values of *W* for cases when the steepness of the longer waves traveling opposed to the wind waves was greater than 0.01 and relatively larger values of *W* when the steepness was less than 0.01.

[41] In order to investigate any possible effect of the steepness of opposing swell on *W*, it was necessary to use only those values of *W* when the wind waves were in fact propagating in the opposite direction to the swell. However, as stated above, there were only a limited number of wave spectra where a peak frequency associated with wind-generated waves could be clearly identified. Therefore wind direction was used as a substitute for wind wave direction when classifying the relative directions of swell waves and the wind waves. Directional differences between swell waves and wind direction of between 110° and 180° were deemed as conditions of opposing swell. Of the 87 data points in Figure 9, a total of 77 were classified as data points from conditions of opposing swell, and these are plotted in Figure 10. These 77 data points are further divided into two categories. Data points depicted as diamonds indicate values of *W* measured when the steepness of the long swell waves was less than 0.01. The dots indicate values of *W* measured when the long swell wave steepness was greater than 0.01. Above wind speeds of approximately 7.5 m s^{-1}, there was a relative lack of values of *W* from seas with long wave steepness greater than 0.01. However, below 7.5 m s^{-1}, there seem to be two distinct regimes of values of *W* which can be explained by swell wave steepness. Steep swell waves appear to have reduced the majority of *W* values observed at wind speeds below 7.5 m s^{-1}. Figure 10 suggests that the steepness of longer waves had a measurable effect on *W* at low wind speeds in this study, but it is clear that this observation needs more investigation with better directional classification of wind waves and an even larger data set of *W*. Given that swell steepness values exceeded the critical value of *Mitsuyasu and Yoshida* [2005] of 0.01, the coastal location of MVCO could provide a suitable site at which to investigate the interaction of wind waves and opposing swell. In further field studies striving to verify the laboratory observations of swell wave/wind wave modulation, concurrent measurements of ocean wave spectra and *W* could provide an excellent representation of one of the possible sources of spectral energy flux, i.e., energy dissipation through wave breaking.

3.3.3. Wave Age Dependence of *W*

[42] One of the goals of this study was to investigate the relationship between *W* and wave age. Wave age is the ratio of the phase speed of the wave components at the spectral peak frequency (c_p) and U_{10}. Often U_{10} is replaced by the wind friction velocity u_*. In cases of fetch-limited conditions, a wide range of sea states can be expected to exist at a given wind speed [*Young*, 1999]. In cases of pure wind seas in the absence of swell, wave age is considered to be a good measure of sea state [*Young*, 1999].

[43] The use of wave age requires that the spectral peak frequency of the locally generated wind waves is known. This therefore limited our study of the relationship between *W* and wave age to the 14 values of *W* for which peak frequencies could be attributed to locally generated wind waves. Figure 11 shows *W* plotted against wave age for

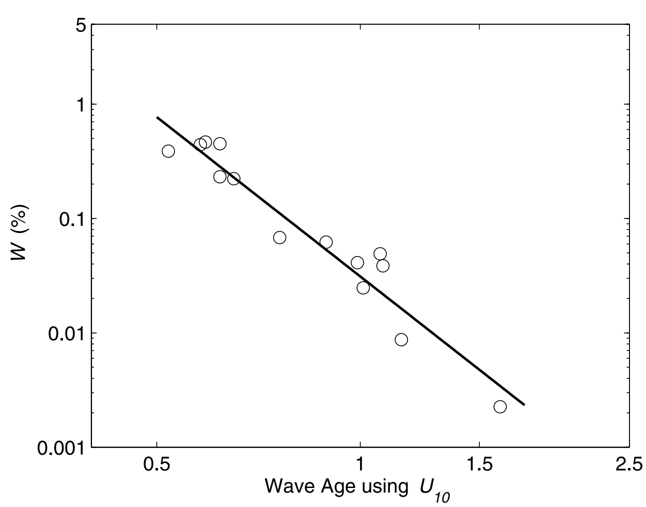

Figure 11. *W* against wave age using U_{10}. The solid line is the power law regression on the data.

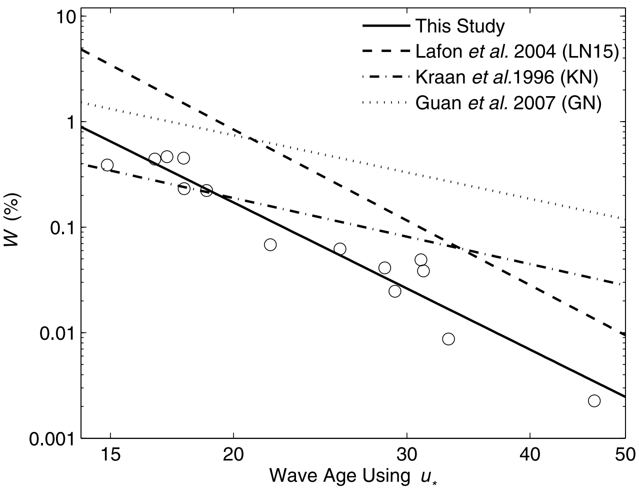

Figure 12. *W* against wave age using wind friction velocity u_*. The solid line is the power law regression on the data. The dashed line is LN15, the dotted line is GN, and the dash-dot line is KN.

those 14 values with well-defined peaks corresponding to locally generated wind waves. The solid line represents the least squares power law fit to the data, and the resulting regression relationship with the r^2 value is

$$W = 0.0311 \times \left(\frac{c_p}{U_{10}}\right)^{-4.63} \qquad r^2 = 0.93. \tag{3}$$

[44] The plot indicates that *W* varied inversely with wave age for this study. It should be noted that there was a much larger range of values for U_{10} (3.10 to 10.75 m s^{-1}) than for c_p (4.76 to 6.21 m s^{-1}). Notwithstanding the excellent correlation between wave age and *W* in equation (3), given the much smaller range of values of c_p in comparison to the range of values of U_{10}, it is difficult to evaluate the effectiveness of wave age as a parameter for modeling *W* in this study. The high correlation is probably due to the even better correlation between *W* and U_{10}, as given in equation (1).

[45] As stated above, wave age can also be parameterized in terms of u_*, in place of U_{10}. In fact, other published models of *W* to wave age parameterizations use u_* in place of U_{10} [e.g., *Kraan et al.*, 1996; *Lafon et al.*, 2004; *Guan et al.*, 2007]. In order to directly compare the *W* to wave age relationship from this study to those previously published, U_{10} was converted to u_*. The drag coefficient C_D used in the conversion was that given by *Large and Pond* [1981], where C_D = 0.0012 for wind speeds between 4 and 11 m s^{-1}. For this study, we also applied this drag coefficient to those wind speeds less than 4 m s^{-1} for simplicity. Figure 12 shows the resulting *W* to wave age relationship using u_* (solid line), and the resulting regression with r^2 value is

$$W = 1.81 \times 10^5 \left(\frac{c_p}{u_*}\right)^{-4.63} \qquad r^2 = 0.93. \tag{4}$$

[46] The *W* to wave age models of *Kraan et al.* [1996, hereinafter referred to as KN] (dash-dot line), *Guan et al.* [2007, hereinafter referred to as GN] (dotted line), and *Lafon et al.* [2004] (dashed line) are included in Figure 12. In the study of *Lafon et al.* [2004], three models are given to represent their *W* to wave age data. We use the relationship given for wave ages greater than 15 only, which corresponds to the range of wave ages encountered in this study. This is equation (18) in their study and is referred to as LN15 in further discussions.

[47] It is clear from Figure 12 that of the four different models, there are two distinct slopes. The solid line representing this study and the dashed line of LN15 are both empirical models based upon measurements of *W* in a coastal zone, and they have the steepest slopes. The remaining two models of KN and GN were both derived on theoretical grounds that whitecapping represents wave energy dissipation. The theoretically derived power law slopes of KN and GN are less steep than those of the empirical studies. The scaling factors were then determined by fitting these models to empirical data.

[48] While the slopes of LN15 and this study are similar, LN15 overestimates the data from this study. This may be attributed to the extremely low fetch conditions that correspond to our data points. Wind direction was from between 14° and 59° from the north. This corresponds to a very small fetch with a maximum value of approximately 6 km. LN15 was derived from measurements of *W* at a fetch of approximately 60 km. As shown in Figure 1d from the paper by *Melville and Matusov* [2002], *W* typically increases with increasing fetch. Before commenting on the differences between our empirical model and the two theoretical models, we discuss the similarities and differences between KN and GN.

[49] While the power law slopes in both KN and GN were derived using similar but not identical theoretical approaches, there is a large discrepancy between values of *W* predicted by both models for a given wave age. We believe this can be explained by examining the data sets of *W* that were used in both studies to determine the scaling factors of the models. In the study of *Kraan et al.* [1996], measurements of *W* were composed of stage A whitecaps only. In the terminology of *Monahan and Lu* [1990], the foam produced by actively breaking waves is called a stage A whitecap. The residual foam left on the sea surface after the wave has broken is termed a stage B whitecap. Stage A and stage B whitecaps represent very different regimes in the evolution of a whitecap. The stage A whitecap represents the process of active breaking and hence energy dissipation. *Guan et al.* [2007] determined their scaling factor using the *W* data set of *Lafon et al.* [2004], which, unlike *Kraan et al.*'s [1996], represents measurements of both stage A and stage B whitecaps. In light of this, it would be expected that GN predicts higher values of *W* for a given wave age than KN.

[50] The differences in slope between empirical and theoretical studies may be explained by discussing the evolution of a whitecap. Assuming that only the actively breaking wave is responsible for energy dissipation, then measurements of stage A whitecaps could be related to energy dissipation. Stage B whitecaps represent the foam patch produced after the wave has broken, and therefore a composite value of *W* from both stage A and stage B whitecaps would not be expected to represent well the

process of active energy dissipation. Because of the difficulty in distinguishing stage A whitecaps from stage B whitecaps in image processing, measurements of *W* in both this study and that of *Lafon et al.* [2004] represent whitecaps of both stages of evolution. Very little quantitative information is available on the comparative areas of stage A whitecaps and stage B whitecaps, but stage B occupies a larger area of white water than stage A and for a longer time. *Monahan and Lu* [1990] estimated that at any instant in time, the fraction of the sea surface covered by stage B whitecaps is about 9 or 10 times greater than that of stage A whitecaps. However, if the area of a stage B whitecap were a nonlinear function of the area of a stage A whitecap, then this could explain the differences in slope between the theoretical models and observed empirical relationships. Further work is needed to investigate and quantify the relative areas of stage A and stage B whitecaps.

3.4. Applicability of Results to the Open Ocean

[51] It is the goal of this paper to highlight a variety of processes that contribute to scatter in *W* values and not to provide another parameterization of *W*. Therefore while equations (1) and (2) (section 3.3.1) and equations (3) and (4) (section 3.3.3) would be suitable for coastal areas of very limited fetch, it may not be appropriate to apply the resulting relationships from this study to open ocean conditions. However, we believe that this study has highlighted some of the processes which need to be taken into account when performing investigations into *W* in the open ocean other than U_{10} measurements alone. As in the coastal zone, the open ocean wavefield may consist of both the locally generated wind waves and swell waves. In this study, the presence of swell increased data scatter and appeared to have reduced values of *W*. Therefore measurements of the wave spectrum would provide an invaluable and complete description of the wavefield, aid in interpretation of *W* values, and also provide a measurement of the slope of the swell waves. The acquisition of wave spectra also allows the accurate estimation of wave age which has been shown to reduce scatter in other *W* studies [e.g., *Lafon et al.*, 2004, 2007; *Sugihara et al.*, 2007]. With the ever-increasing capacity for data storage, *W* values should be the result of averaging over hundreds of images rather than tens of images. This is applicable to any further *W* studies, both in the coastal zone and in the open ocean. A knowledge of the tidal regime at the MVCO coastal site enabled conspicuously high values of *W* to be explained; therefore where possible, tidal effects should also be considered when performing *W* studies in the open ocean.

4. Conclusions

[52] Measurements of percentage whitecap coverage *W* in a coastal zone with limited fetch conditions have been presented. An automated image-processing method allowed over 100,000 images to be processed for *W*. This allowed a minimum of 400 images to be analyzed for each single value of *W*. An investigation into the convergence of *W* values with increasing image numbers showed that using a minimum of 300 images provided estimates of *W* within about ±4% of the mean *W* value of 1200 images taken in a 20 min period. The acquisition of wave spectra enabled an assessment of the wavefield characteristics for the measurement period. From an initial plot of *W* against U_{10}, a combination of the relatively large number of values of *W* and wave spectrum measurements enabled much of the scatter to be explained. This demonstrates the value of having a large data set of *W* measurements which are the composite of hundreds of images and the importance of having coincident wave spectrum measurements.

[53] This study highlighted the influence of fetch, tidal currents, and wavefield characteristics on values of *W* in a coastal zone. The limited fetch conditions due to the location of the measurements and wind direction explain the low values of *W* in comparison to other published data sets. The presence of eastward tidal currents in directional alignment with a westerly wind appear to have enhanced wave breaking, which resulted in larger values of *W*. This feature was observed on two separate occasions at both low wind speeds (circa 4 m s^{-1}) and moderate wind speeds (circa 11 m s^{-1}). We also found that data scatter in *W* to U_{10} relationships was larger when seas were swell dominated than at times when seas were mixed. This may be in part due to the fact that waves break preferentially at the crests of longer waves. Thus any *W* to U_{10} relationship would be expected to exhibit more scatter in the presence of longer swell waves. Similarly to *Sugihara et al.* [2007], we found that swell-dominated seas resulted in overall lower values of *W* than in mixed seas. For specific conditions of opposing swell waves of steepness greater than 0.01 coexisting with wind waves, we found that *W* was reduced at wind speeds less than 7.5 m s^{-1} in comparison to conditions when swell steepness values were less than 0.01. These swell effects are expected to be enhanced in the coastal zone as the longer waves begin to interact with the bottom and steepen. Further experiments and larger data sets are needed to clarify this apparent effect. Because of the shallow depth of the measurement site which causes the long swell waves to slow down and steepen, the ASIT at MVCO is an ideal location to investigate the effects that long waves have on the growth and energy distribution of shorter waves. The coastal site acts as a type of natural laboratory where many processes, such as periodic tidal currents and swell wave steepening, are more evident than in the open ocean and whose effects on *W* can be more readily investigated. The uncharacteristic lack of scatter in *W* from mixed seas in this study suggests that with large number of images, accurate wind speed-only parameterizations of *W* may be possible when *W* is minimally influenced by other factors such as swell waves or tidal currents.

[54] It is clear that a wide range of physical and environmental factors combine to determine *W* in a coastal zone. While we tried to explain the scatter in the original data set, there are other factors that may affect *W* which were not evaluated in this study. The temperature of the water may affect both the onset of breaking and the persistence of stage B whitecaps through viscous effects, and atmospheric stability could also influence *W*. The presence or absence of surfactants on the water's surface may provide a stabilizing effect for bubbles, hence prolonging the lifetime of stage B whitecaps. Image acquisition, ADCP measurements, and wind measurements were not colocated. Direct measurement of the turbulent fluctuations of the wind at the image acquisition site would facilitate the direct calculation

of u_*, which has been noted in other studies [e.g., *Lafon et al.*, 2004; *Wu*, 1988] as possibly providing a more accurate parameterization for W than U_{10}.

[55] As long as whitecap coverage models are being used as inputs to aerosol flux models and in atmospheric correction algorithms for the retrieval of ocean color, there is a need for larger image data sets and concurrent measurements of the wave spectrum from which to further constrain the causes of scatter in W. It is only when the causes of scatter are more completely understood that more robust models of W can be developed.

[56] **Acknowledgments.** This work was completed while Adrian Callaghan was a guest of Grant Deane and Dale Stokes at the Innovative Marine Technology Laboratory at the Scripps Institution of Oceanography, University of California, San Diego as part of the University of California Education Abroad Programme (UCEAP). Funding for this visit was obtained from the UCEAP, the Martin Ryan Institute at the National University of Ireland, Galway and the Marine Institute, Ireland via the National Development Plan, 2000–2006 Marine RTDI Measure. Much appreciation is expressed to MVCO for the use of their archived data. The SPACE02 research was supported by the Office of Naval Research, grant N00014-04-1-0728.

References

Anguelova, M. D., and F. Webster (2006), Whitecap coverage from satellite measurements: A first step toward modelling the variability of oceanic whitecaps, *J. Geophys. Res.*, *111*, C03017, doi:10.1029/2005JC003158.

Asher, W. E., L. M. Karle, B. J. Higgins, P. J. Farley, I. S. Leifer, and E. C. Monahan (1996), The influence of bubble plumes on air-seawater gas transfer velocities, *J. Geophys. Res.*, *101*, 12,027–12,041, doi:10.1029/96JC00121.

Asher, W., J. Edson, W. McGillis, R. Wanninkhof, D. T. Ho, and T. Litchendorf (2002), Fractional area whitecap coverage and air-sea gas transfer velocities measured during GasEx-98 in *Gas Transfer at Water Surfaces*, *Geophys. Monogr. Ser.*, vol. 127, edited by M. A. Donelan et al., pp.199–203, AGU, Washington, D. C.

Chen, G., and S. E. Belcher (2000), Effects of long waves on wind generated waves, *J. Phys. Oceanogr.*, *30*, 2246–2256, doi:10.1175/1520-0485(2000)030<2246:EOLWOW>2.0.CO;2.

Chu, J. S., S. R. Long, and O. M. Phillips (1992), Measurements of the interaction of wave groups with shorter wind-generated waves, *J. Fluid Mech.*, *245*, 191–210, doi:10.1017/S0022112092000417.

Dobson, F., W. Perrie, and B. Toulany (1989), On the deep water fetch laws for wind generated surface gravity waves, *Atmos. Ocean*, *27*, 210–236.

Donelan, M. A. (1987), The effect of swell on the growth of wind waves, *John Hopkins APL Tech. Dig.*, *8*(1), 18–23.

Dulov, V. A., V. N. Kudryavstev. and A. N. Bol'shakov (2002), A field study of whitecap coverage and its modulations by energy containing surface waves, in *Gas Transfer at Water Surfaces*, *Geophys. Monogr. Ser.*, vol. 127, edited by M. A. Donelan et al., pp. 187–192, AGU, Washington, D. C.

Frouin, R., S. F. Iacobellis, and P. Y. Deschamps (2001), Influence of oceanic whitecaps on global radiation budget, *Geophys. Res. Lett.*, *28*(8), 1523–1526, doi:10.1029/2000GL012657.

Gordon, H. R. (1997), Atmospheric correction of ocean color imagery in the Earth observing system era, *J. Geophys. Res.*, *102*, 17,081–17,106, doi:10.1029/96JD02443.

Guan, C., W. Hu, J. Sun, and R. Li (2007), The whitecap coverage model from breaking dissipation parameterizations of wind waves, *J. Geophys. Res.*, *112*, C05031, doi:10.1029/2006JC003714.

Hanson, J. L., and O. M. Phillips (1999), Wind sea growth and dissipation in the open ocean, *J. Phys. Oceanogr.*, *29*, 1633–1648, doi:10.1175/1520-0485(1999)029<1633:WSGADI>2.0.CO;2.

Kraan, C., W. A. Oost, and P. A. E. M. Janssen (1996), Wave energy dissipation by whitecaps, *J. Atmos. Oceanic Technol.*, *13*, 262–267, doi:10.1175/1520-0426(1996)013<0262:WEDBW>2.0.CO;2.

Lafon, C., J. Piazzola, P. Forget, O. Le Calve, and S. Despiau (2004), Analysis of the variations of the whitecap fraction as measured in a coastal zone, *Boundary Layer Meteorol.*, *111*, 339–360, doi:10.1023/B:BOUN.0000016490.83880.63.

Lafon, C., J. Piazzola, P. Forget, and S. Despiau (2007), Whitecap coverage in coastal environment for steady and unsteady wave field conditions, *J. Mar. Syst.*, *66*, 38–46, doi:10.1016/j.jmarsys.2006.02.013.

Large, W. G., and S. Pond (1981), Open ocean momentum flux measurements in moderate to strong winds, *J. Phys. Oceanogr.*, *11*, 324–336, doi:10.1175/1520-0485(1981)011<0324:OOMFMI>2.0.CO;2.

Mårtensson, E. M., E. D. Nilsson, G. de Leeuw, L. H. Cohen, and H. C. Hansson (2003), Laboratory simulations and parameterization of the primary marine aerosol production, *J. Geophys. Res.*, *108*(D9), 4297, doi:10.1029/2002JD002263.

Melville, W. K., and P. Matusov (2002), Distribution of breaking waves at the ocean surface, *Nature*, *417*, 58–63, doi:10.1038/417058a.

Mitsuyasu, H., and Y. Yoshida (2005), Air-sea interactions under the existence of opposing swell, *J. Oceanogr.*, *61*, 141–154, doi:10.1007/s10872-005-0027-1.

Monahan, E. C. (1971), Oceanic whitecaps, J. Phys, *Oceanogr.*, *1*, 139–144,doi:10.1175/1520-0485(1971)001<0139:OW>2.0.CO;2.

Monahan, E. C., and M. Lu (1990), Acoustically relevant bubble assemblages and their dependence on meteorological parameters, *IEEE J. Oceanic Eng.*, *15*(4), 340–349, doi:10.1109/48.103530.

Monahan, E. C., and I. O'Muircheartaigh (1980), Optimal power-law description of oceanic whitecap coverage dependence on wind speed, *J. Phys. Oceanogr.*, *10*, 2094–2099,doi:10.1175/1520-0485(1980)010<2094:OPLDOO>2.0.CO;2.

Monahan, E. C., and M. C. Spillane (1984), The role of oceanic whitecaps in air-sea gas exchange, in *Gas Transfer at Water Surfaces*, edited by W. Brutsaert, and G. H. Jirka, pp. 495–503, Springer, Dordrecht, Netherlands.

O'Dowd, C. D., and G. de Leeuw (2007), Marine aerosol production: A review of current knowledge, *Philos. Trans. R. Soc. Ser. A*, *365*, 1753–1774, doi:10.1098/rsta.2007.2043.

Panofsky, H. A., and J. A. Dutton (1984), *Atmospheric Turbulence: Models and Methods for Engineering Applications*, John Wiley, Hoboken, N.J.

Phillips, O. M., and M. L. Banner (1974), Wave breaking in the presence of wind drift and swell, *J. Fluid Mech.*, *66*, 625–640, doi:10.1017/S0022112074000413.

Ross, D. B., and V. Cardone (1974), Observations of oceanic whitecaps and their relation to remote measurements of surface wind speed, *J. Geophys. Res.*, *79*, 444–452, doi:10.1029/JC079i003p00444.

Stramska, M., and T. Petelski (2003), Observations of oceanic whitecaps in the north polar waters of the Atlantic, *J. Geophys. Res.*, *108*(C3), 3086, doi:10.1029/2002JC001321.

Sugihara, Y., H. Tsumori, T. Ohga, H. Yoshioka, and S. Serizawa (2007), Variation of whitecap coverage with wave-field conditions, *J. Mar. Syst.*, *66*, 47–60, doi:10.1016/j.jmarsys.2006.01.014.

Violante-Carvalho, N., F. J. Ocampo-Torres, and I. S. Robinson (2004), Buoy observations of the influence of swell on wind waves in the open ocean, *Appl. Ocean Res.*, *26*, 49–60, doi:10.1016/j.apor.2003.11.002.

Woolf, D. K. (2005), Parameterization of gas transfer velocities and sea-state-dependent wave breaking, *Tellus, Ser. B*, *57*, 87–94.

Wu, J. (1979), Oceanic whitecaps and sea state, *J. Phys. Oceanogr.*, *9*, 1064–1068,doi:10.1175/1520-0485(1979)009<1064:OWASS>2.0.CO;2.

Wu, J. (1988), Variations of whitecap coverage with wind stress and water temperature, *J. Phys. Oceanogr.*, *18*, 1448–1453, doi:10.1175/1520-0485(1988)018<1448:VOWCWW>2.0.CO;2.

Young, I. R. (1999), *Wind Generated Ocean Waves*, *Elsevier Ocean Eng. Ser.*, vol. 2, Elsevier, New York.

Zhao, D., and Y. Toba (2001), Dependence of whitecap coverage on wind and wind-wave properties, *J. Oceanogr.*, *57*, 603–616, doi:10.1023/A:1021215904955.

A. H. Callaghan, Department of Earth and Ocean Sciences, National University of Ireland, Galway, Ireland. (callaghan.adrian@gmail.com)

G. B. Deane and M. D. Stokes, Scripps Institution of Oceanography, University of California, San Diego, CA 92093-0238, USA.